

# The inspection of rupture following 2013 Khaki seismic sequence

Parham Dehghani<sup>1</sup>, Mehrdad Pakzad<sup>2</sup>  
Institute of Geophysics, University of Tehran, Iran

## Abstract

One of the acceptable methods for modelling the seismic source characteristics is through point-source simplification. Although this simplification causes a substantial disparity from the real convoluted nature of an earthquake source process, it can lead to a framework for retrieval of the rupture geometry and source time function. In this study, we exploited point-source approximation compatible with the rupture process for modelling the predominant faulting geometry caused by the initiation of Khaki seismic sequence. First, all recorded earthquakes over six months after the main shock, 2013 April 9th, in vicinity of khaki anticline, near to city of Shonbeh, were relocated implementing the probabilistic nonlinear method based on Bayesian inference. The synthetic test was done having on hand the exact distribution of real stations. Thus the proper value for the parameter that can explicitly affect the error results was modeled to be 0.01. After performing relocation task, 98 relocated events with horizontal errors of less than 5 km from all 373 recorded events were taken into account for further analysis of the spatial characteristics of the sequence. In advance, point source inversion was implemented for 21 events greater than 4.5 Mn. Then, supplementary investigations and stability test were performed for the results of the main shock. Thus, we were convinced that the gathered results are reliable enough to be used for the seismotectonic analysis of the region resulted by the sequence. Eventually the reverse slip vector with substantial left-lateral strike slip component (in some cases) was modeled exploiting the distribution of inverted centroids and resulted faulting geometry for the chosen events. A southward dip of the probable causative fault was seen, furthermore depth range of the rupture was localized ranging from 8 to 12 Km in the lowermost part of the sedimentary cover.

**Keywords:** point-source, ISOLA, Bayesian Theory, Nonlinear Probabilistic Location, Central Zagros, Bushehr

---

<sup>1</sup> p.dehghani@ut.ac.ir

<sup>2</sup> pakzad@ut.ac.ir

# 1 Introduction

On April 9th 2013 16:22 local time, an earthquake of 6.1 Mn and 6.3 Mw hit Dashti, more precisely Shonbeh small city, based on Institute of Geophysics of University of Tehran (IGUT) report. Epicenter was reported to be 16km far from Kaki, 27km far from Khormoj and 90km far from Bushehr. Although epicenter was close to Bushehr nuclear plant, this critical unit remained undamaged based on the investigations afterwards. The most damages were revealed in small city of Shonbeh and 23 close villages. This damage was estimated to ruin 10000 people over the region. Moreover, a 5.2 Mn earthquake (12:29 local time, April 10th) struck Dashti again and damaged a bunch of people and facilities over the region. To be more precise, this seismic sequence following 6.1 Mn main shock included 372 aftershocks greater than 3.00 Mn. The phase information was recorded from numerous resources including IGUT, IIEES and some Arabic station over 6 months the main shock hit the region.

In this study, we would precisely explore this seismic sequence. First, relocation of the events is performed using Nonlinear Bayesian method. Afterward, seismic point source inversion of the main shock is reached. Furthermore, a comprehensive discussion on the stability of the results is presented. Finally, seismotectonics induced by the sequence is concluded and suggested.

## 2 Seismotectonics of the Region

Area of interest is located in Zagros seismotectonic province. It is limited to the Mountain Front Fault (MFF) to the northeast, and to the Zagros Foredeep Fault (ZFF) to the southwest. Zagros seismotectonic province includes different morphotectonic regions [1] from which Zagros Foredeep region is pertinent to the area of interest in this study. Some of the important fault systems affect tectonics of the region as below:

### **Mountain Front Fault (MFF)**

This fault is a discontinuity between Zagros Simply Folded Belt (ZSFB) and High Zagros (HZ). It is considered as one of the crucial hidden fault systems over the region with northward dip and dominant reverse slip.

### **Zagros Foredeep Fault (ZFF)**

It is located parallel to MFF at the height of about 100 meters from the sea level, and separates Zagros Foredeep region from Zagros Coastal Plain [1].

### **Kazerun Fault**

This fault is 450 km length with dominant right lateral strike slip mechanism, and lies on north-south direction. It is located within the seismogenic part of whole Zagros seismotectonic province, and can be distinguished 15 km far away Kazerun city.

### **Borazjan Fault**

This fault is located southwest of Kazerun Fault with 180 km overall length. The dominant mechanism of the tectonics it induces is reverse slip. Consequently, most of the strike-slip tectonic activities are absorbed by Kazerun fault system.

### **Karehbas Fault**

This fault is located 90km east of Bushehr area and is about 130km length. Also its tectonic mechanism is reverse like most of the faults over this region. More than 109 seismic events with magnitude greater

than 5 occurred within the region of study over 100 years ago. This explicitly depicts the high rate of seismicity over this region [2]. Furthermore, inspections revealed more than 10 deadly events that took place from 1500 to 2000.

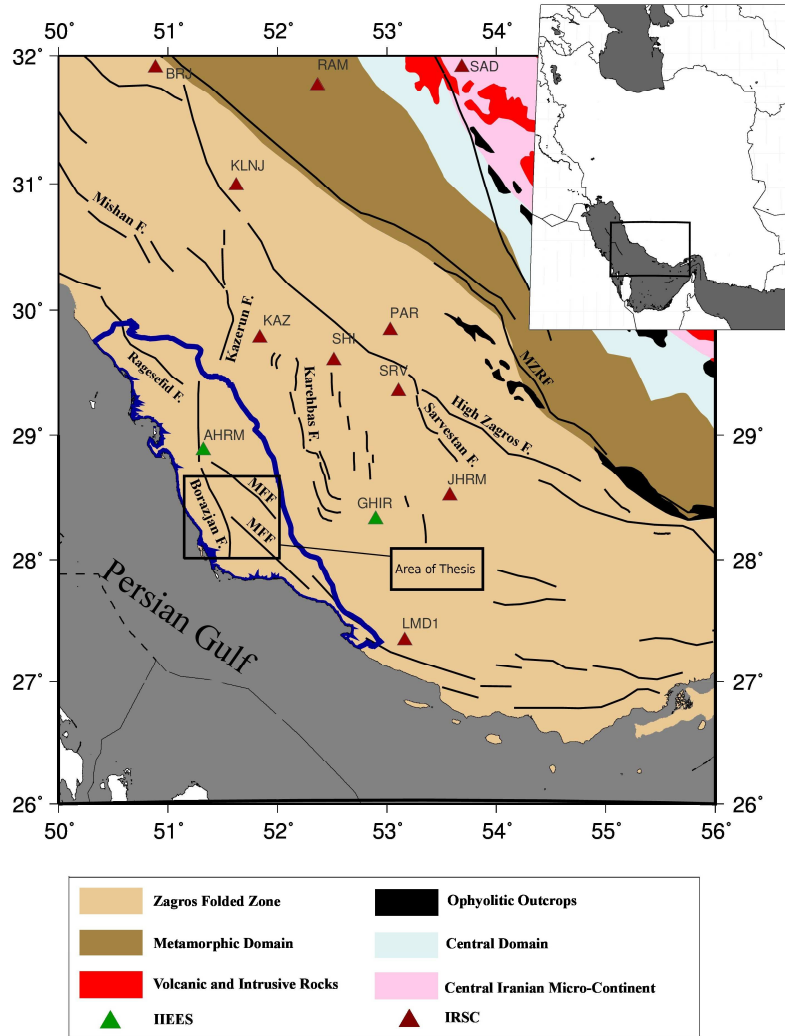


**Figure 2.1.** Area of study including IIEES and IRSC seismic stations.

## 3 Results and Discussions

### 3.1. Relocation of the seismic sequence

#### 3.1.1. Area of study and gathered data

In this study we first will attempt to relocate 373 seismic events greater than 3.00 Mn over the region located within latitude 27.5 to 29.5 and longitude 50.5 to 52.5 exploiting nonlinear probabilistic method [3]. To improve recorded phases and diminish azimuthal gap, we employ data recorded in IGUT, IIEES and some Arabic stations. Regarding far distance between most of the stations and area of the study, we use Sg, Sn, Pg and Pn phase data. Three dimensional grid we used for relocation task is centered at 28.57 N latitude and 51.97 E longitude, and contains all the stations that are 600km distant eastward, westward, northward and southward from the center. This three dimensional grid features 130km depth from the ground to compute the velocity model and consequent travel times to each station. In figure 3.1.1, all the

stations of IIEES, IGUT and foreign ones within this grid can be seen. Phase data of these stations is exploited to perform nonlinear relocation process.

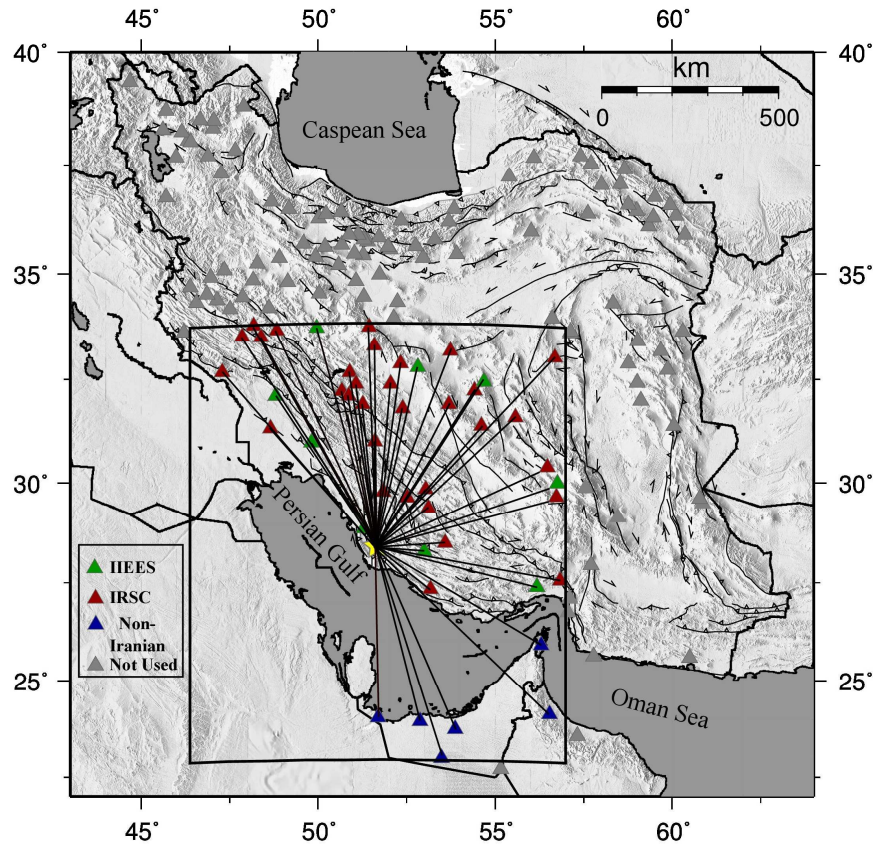


**Figure 3.1.1.** Exploited seismic station to build travel time grid.

### 3.1.2. Optimization of the parameters

One of the present methods to estimate real errors in an inverse problem is to forward modelling using known data and take back to inverse problem (here relocation of seismic events) to find the solution and real errors. Importance of this approach gets higher when all the features or variables affecting the solution of a forward problem cannot be theorized and expressed in the language of mathematics. More crucial problem is to seek a realistic complex three dimensional earth model that can yield forward solutions comparable with real data. To be realistic, this complex model of the earth is not accessible, in result an approach has to be proposed to estimate real errors (not modelled errors). Importance of real error estimation increases facing the inverse problem of seismic event depth. With reliable depth estimation on hand, rupture analysis and revealing seismogenic zone can be performed with higher certainty.

In this section, we seek optimized value of LocGau2 parameter by artificial hypocenter inversion of the known events using all the stations shown in Figure 3.1.1. This parameter considerably affects the result of inversion and the errors, then more conservative choice of its value can improve the result of relocation process. Furthermore, a Gaussian error with standard deviation of 0.1 second is considered as Pg and Pn phase picking error.

To build artificial events, 5 vertical profile of events with 20 nodes each ranging from 1km depth to 39 km depth with 2km vertical distance are considered. The central profile is put to the center of relocation

grid, and other 4 profiles are set to be 4km distant in 4 directions (east, west, north and south) from the center. We employ Time2EQ package of NonLinLoc program [3] for the calculation of travel times. The one-dimensional velocity model of Hatzfeld [4], retrieved from local events for central Zagros, is exploited. Furthermore, 42 stations, exactly like the main shock, are used to build travel times of Pg and Pn phases considering 0.1s Gaussian error of phase picking.

After the calculation of travel times for all events and stations, inverse problem of finding hypocenter of all events is performed while different values of LocGau2 ranging from 0.005 to 0.05 are examined. Finally, to inject the crucial effect of untrue velocity model of the earth, then its systematic error, new velocity model used in IGUT is employed to perform inversion task.

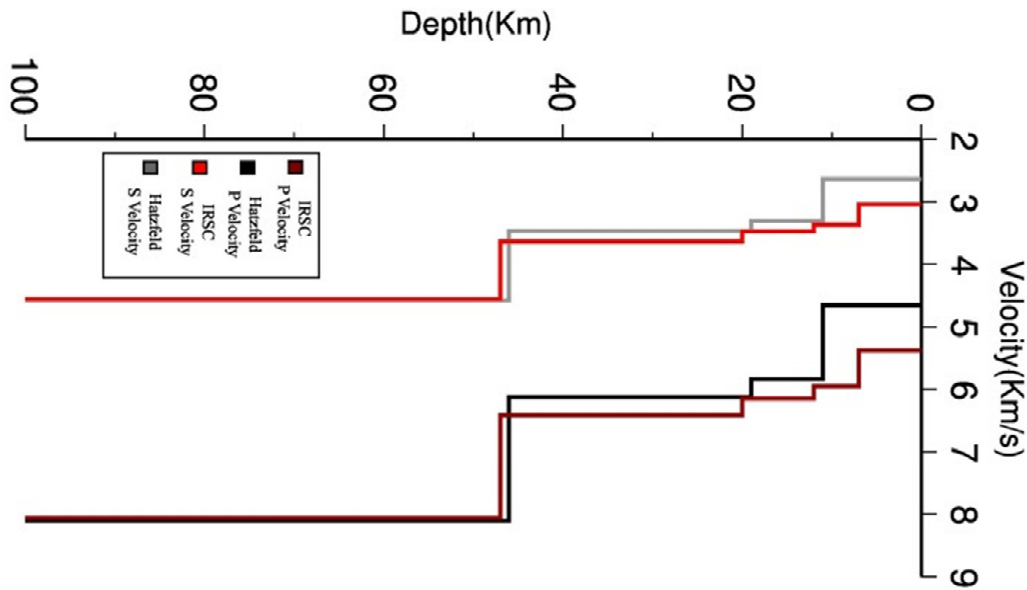


**Figure 3.1.2.** Hatzfeld and IRSC one-dimensional velocity model in comparison.

Real versus modeled errors are gathered due to each LocGau2 parameter shown in histogram for all artificial events, as seen in figure 3.1.3. In this figure, both real and modeled errors of epicenter and depth are depicted for all 100 artificial events as one histogram for each value of LocGau2 parameter. As seen in the figure, modeled errors deviate from real errors considerably as LocGau2 parameter increases, so that heightened value of this parameter cannot truly lead to modeled solutions close to real ones.

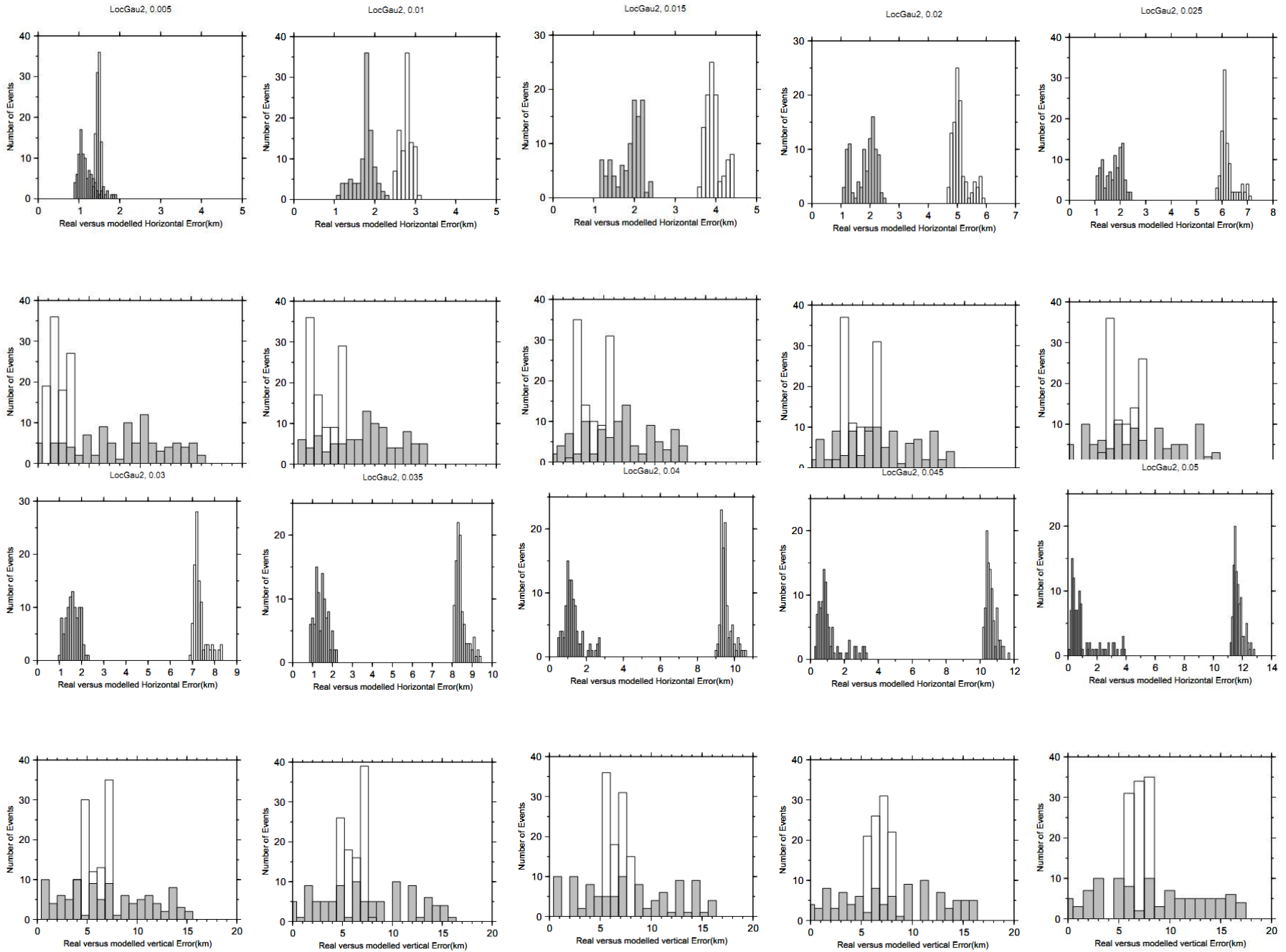


**Figure 3.1.3.** Histogram of real and modeled errors relevant to different LocGau2 values. Gray bars showing real errors versus uncolored bars showing modeled errors.

Considering departure of modeled and real errors, LocGau2= 0.01 would be a reasonable choice, as true in the most of studies and regions. Inputting this value, relocation of all artificial events are performed, and the result is shown in the figure 3.1.4. It is worth to note that we consider the average model as final solution over the probabilistic distribution of all sampled models. Reason is the importance of the variation of probability of each model in the vicinity of optimum one. To diminish unsystematic error over the inversion process, considering the sampled models variations comparing to optimum model is obligatory, as local maxima can mislead us to an untrue solution. This circumstance comes up when the final probabilistic distribution is not bell-shaped, and there would be some local maxima, so that solution with maximum probability cannot certainly lead to the true solution that is comparable to the real optimum model.

Noting figure 3.1.4, some discussions have to be presented. First, we succeed to invert for the epicenters with high accuracy and small real errors while trying to simulate real situation (different forward and inversion earth models). Most of the events are relocated with the epicentral error smaller than 2km. One another noticeable fact is that none of the events are relocated within first 12km depth (figure 3.1.4 E and F).

As seen in figure 3.1.2, there is a high contrast between P-wave velocity in two models. IRSC velocity model features considerably higher P-wave velocity comparing to Hatzfeld model. In consequence, sampled models tend to deeper locations to compensate for travel time discrepancy present in forward modeling using Hatzfeld velocity model. This fact shows the high impact of true velocity model of the earth that is in affinity to real earth to result certain locations.

As there is high affinity of the region of study to Hatzfeld velocity model and the fact that depth of sedimentary cover in the region is about 12km [5], we choose to exploit Hatzfeld model as one to relocate Khaki seismic sequence. Although it would not be a reasonable choice for waveform modeling, as this velocity model is more like a local distribution of earth layers contemplating its geographical extent. Hatzfeld model comes with less details comparing to IRSC one, so that we will manipulate IRSC model for waveform modeling later in this study.

### **3.1.3. Relocation of the events over region of study**

In this section, 373 seismic events of Khaki sequence are relocated employing optimized values of the efficient parameters, e.g. LocGau2. All the events are gathered over 6 months after the main shock, and their phase data are retrieved from IRSC, IIEES and some Arabic stations. As said before, NLLOC is employed using EDT probability function that diminishes the unwanted effect of untrue arrival times. Moreover, we choose events with at least 15 phase data including S and P waves' data as the ones to be relocated. As sampling method, Oct-tree [3] is employed for its pace and accuracy to seek for global maxima versus local ones. Resulted depth and epicentral errors, retrieved from covariance matrix of sampled points, are shown as histogram in figure 3.1.5 A.

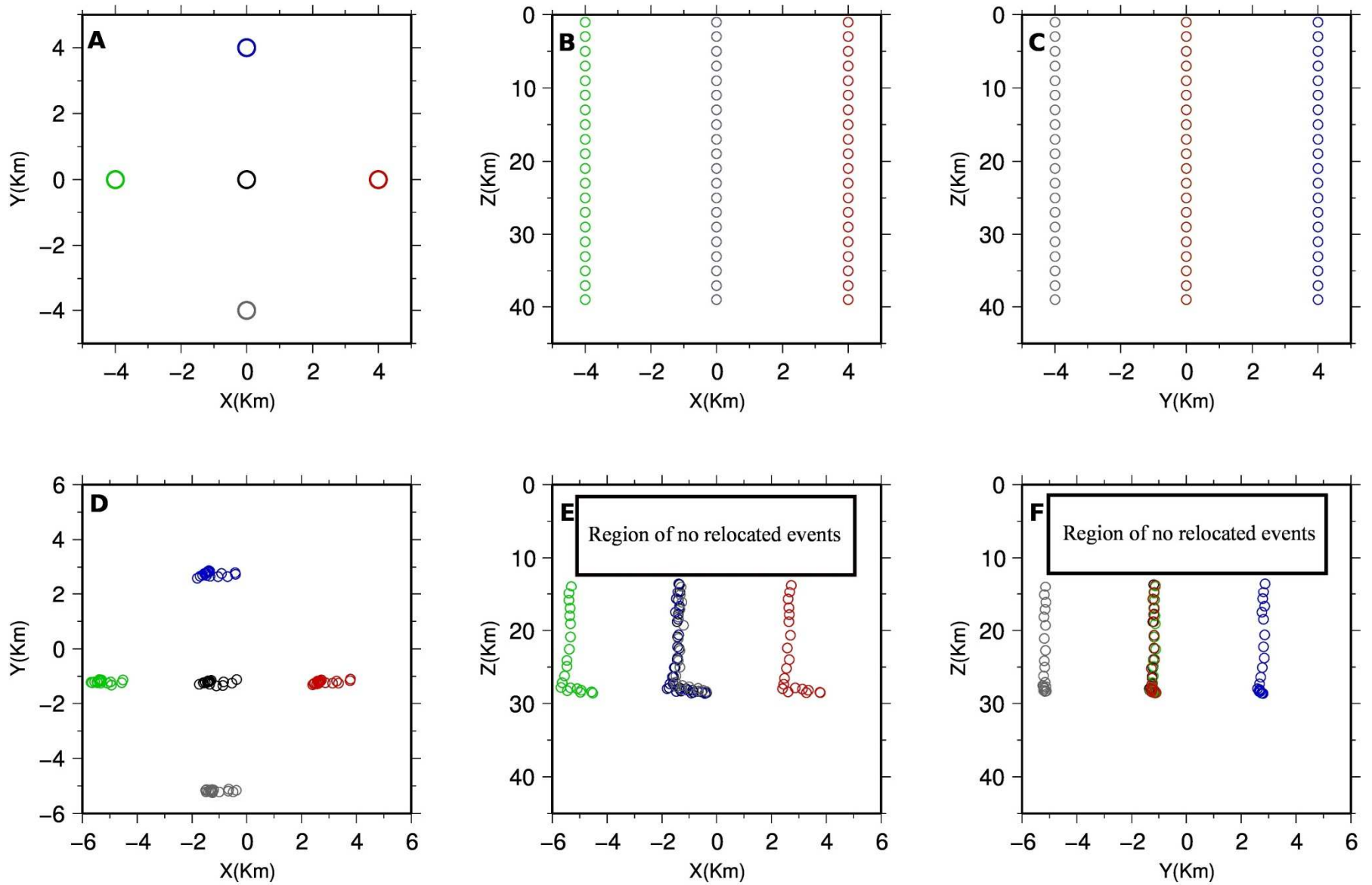


**Figure 3.1.4.** Relocation results of all artificial events considering  $\text{LocGau2}=0.01$ . A, B and C depict events at their real positions versus D,E and F showing relocated events.

Looking at figure 3.1.5 A, most of the relocated events feature the epicentral error less than 5km. Likewise depth errors of most of the events are calculated less than 5km. Although the question of how similar is the Hatzfeld model and real earth remains unanswered. So that depth modeled errors cannot be compared to real errors with high certainty. Considering 3.1.5 B, distribution of the stations can be investigated. Most of the relocated events feature azimuthal gap less than 160 to 180 degrees, showing the impact of Arabic stations. Furthermore no explicit deviation of secondary azimuthal gap comparing to primary azimuthal gap is seen, suggesting uniform distribution of the stations and the fact that loss of none of the stations phase data can considerably affect the results.

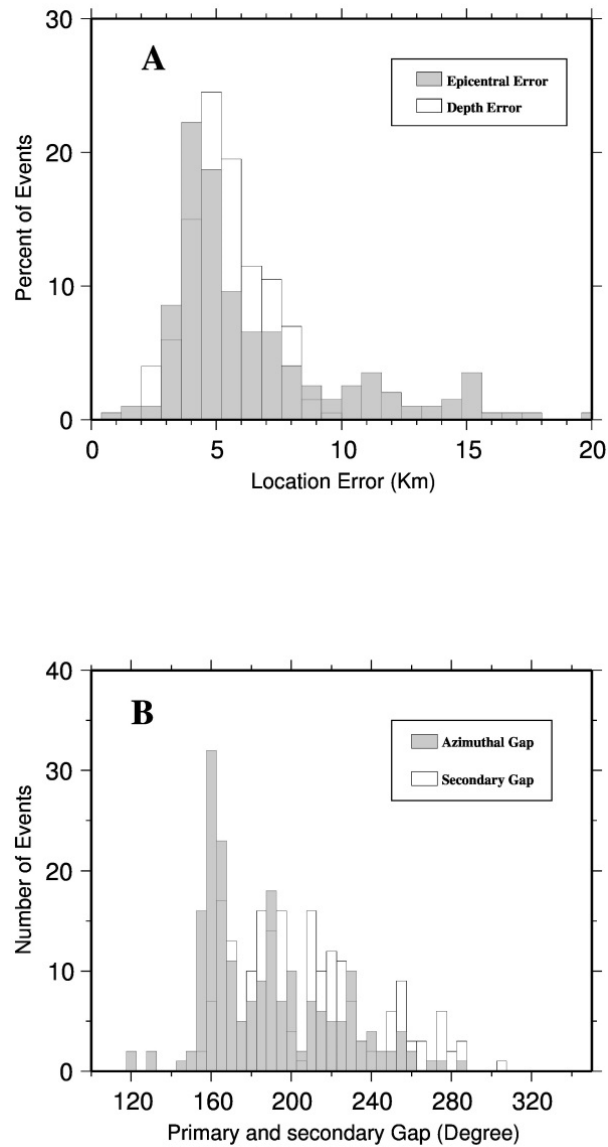


**Figure 3.1.5.** Histogram of epicentral and vertical errors accompanied by primary and secondary gaps for the relocated events. A shows the epicentral and vertical errors and B depicts primary and secondary gaps pertinent to the result of relocation for the events.

In figure 3.1.6, distribution of the sampled models for the main shock and its biggest aftershock can be seen. To clarify the scattered points, we choose one model from each 7 models over the model space. USGS and IRSC solutions are depicted along average model and most probable model in the figure. As

explicitly seen, distribution of the models mostly confines to 68-percent ellipse, volume with 68 percent probability to happen as the hypocenter of an event. This alone shows that distribution of the sampled points based on their probability to happen is statistically Gaussian. In result, expressing the modeled errors using covariance matrix is reasonable and trustworthy. As mentioned before, average solution is the best choice as the output of a probabilistic distribution for each event, and one standard deviation can be regarded as the error of 68-percent probability of happening.

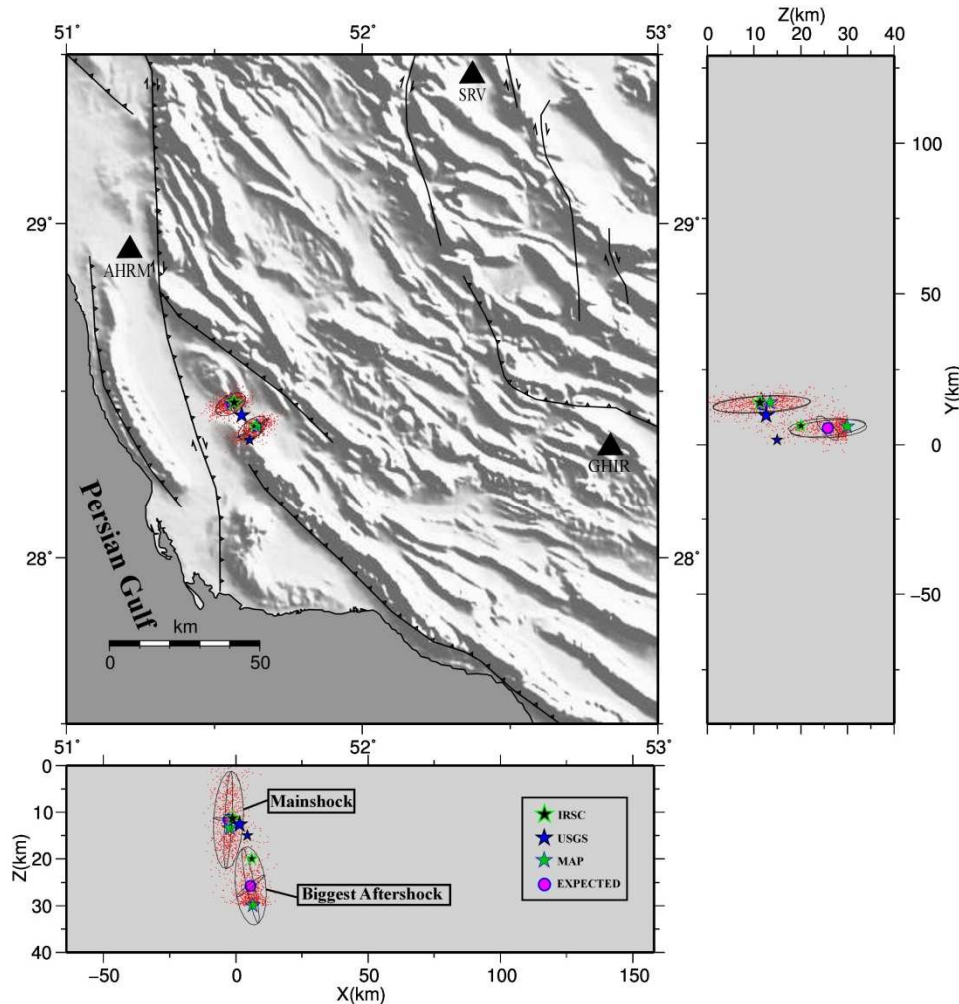


**Figure 3.1.6.** Distribution of the scatter points for the main shock and its biggest aftershock to reach final probability density function.

To grasp the time and geographical migration of the sequence, events with epicentral error less than 5km and happened up to 30 days after the main shock are colorized based on their time of happening relative to the main shock (figure 3.1.7). Main shock epicenter is relocated close to Khaki anticline. As this place is near to Shonbeh city, damages must be considerable in this city as it is in reality. Considering spatial and time distribution of the aftershocks up to 30 days after the main shock, a northwest-southeast trend can be explicitly distinguished. Although much of the seismic activity is concentrated on the northwestern part, aftershocks tend to southeast as time goes on. For the loss of redundant aftershocks in the southeastern part, this part cannot be regarded as a new seismically activated region.

Investigating depth distribution of the aftershocks in figure 3.1.7, concentration of events over depth range of 15 to 30km with steep dip (figure 3.1.8 b) can be viewed, based on histogram presented.

Contemplating many studies suggesting depth of sedimentary cover in ZSFB as 8 to 12km [6,7,8] , occurrence of the aftershocks in the bedrock can be concluded. Also main shock depth is 12km suggesting that it occurred at the upper-most part of the bedrock in the vicinity of sedimentary cover. To verify this argument within over studies, it is worthy to review the depth range of seismic events over ZSFB to be concentrated in the bedrock. Furthermore, rupture would be probably aseismic in the sedimentary cover, e.g. shortening, so that occurrence of the aftershocks in bedrock is certainly reasonable.

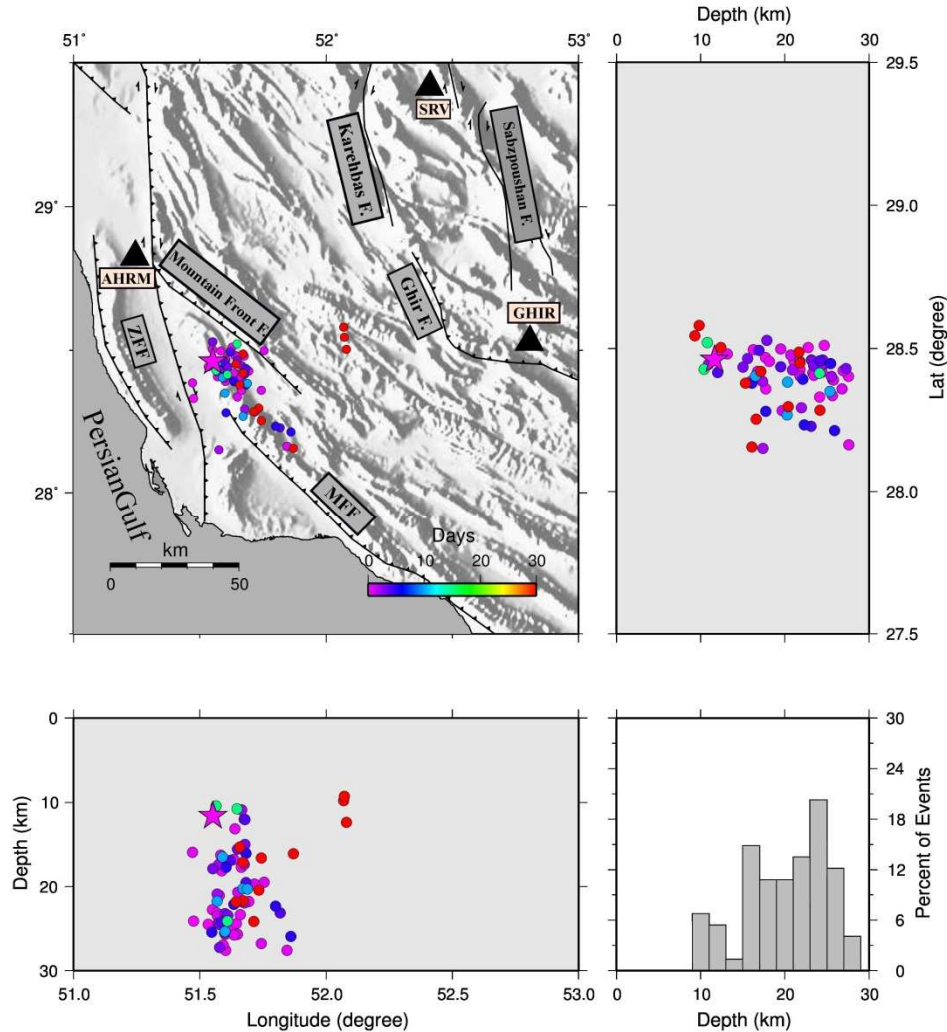


**Figure 3.1.7.** Colored events within 30 days after the main shock accompanied with the histogram of their depths.

To investigate spatial migration of the events further, two sections with 60 and 135 degrees azimuth are taken in figure 3.1.8 a and b. All the relocated events are projected onto these planes, in result a steep dip of about 70 degrees for the probable causative fault is seen (figure 3.1.8 a). This dip is in accord with 50-60 degrees of most of the seismically active faults over ZSFB. To be added, migration of the aftershocks to southeast and upper-most part of the bedrock can be concluded (3.1.8 b).

### 3.2. Seismic source waveform modeling for important events

Focal mechanism inversion for 21 seismic events greater than 4.5 Mn is performed employing Zaheradnik method [9] and regional waveform data. Considering the advantages and output possibilities,

we exploit the new version of ISOLA [10] to reach results. Reader is referred to the paper for being more familiar with new possibilities provided in the new version of ISOLA. Along inversion results, sub-event investigation tfor the main shock is performed and presented. Moreover, stability and certainty of the retrieved focal mechanisms are investigated for 10 chosen events out of 21 ones inverted.

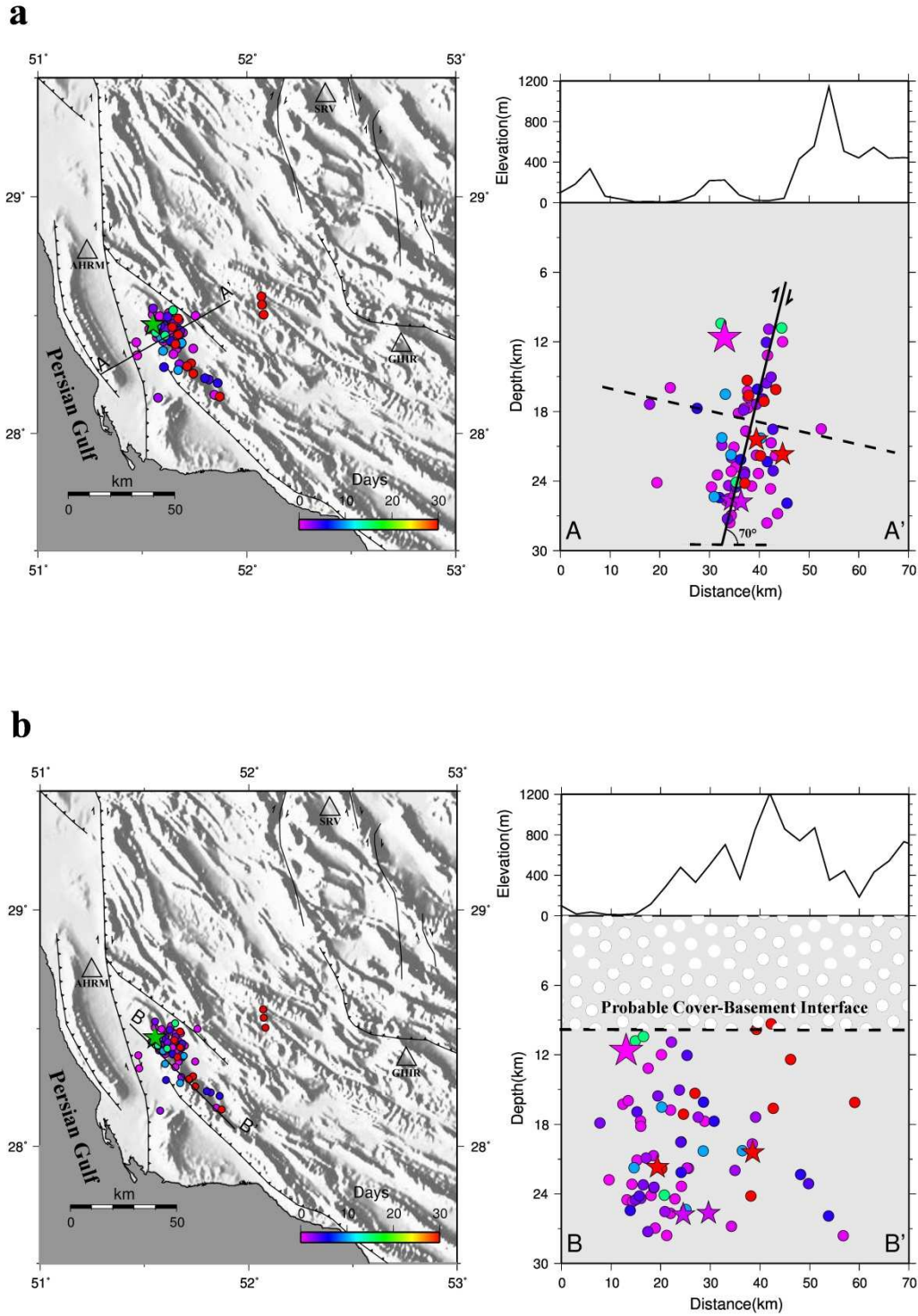


**Figure 3.1.8 a and b.** Relocated events within 30 days after the main shock onto two cross sections (a) 60 and (b)135.

### 3.2.1. Data and velocity model

Waveform data of wide-band stations of IGUT and IIEES is exploited for the inversion task. Almost different stations are used for inversion of each event considering data quality and SN ratio. Overall stations data of AHRM (Ahram), JHRM (Jahrom), SHI (Shiraz) and GHIR (Ghir) are mostly used for the events. Furthermore, Wavenumber method of Bouchon [11] is exploited to calculate green functions. IRSC velocity model is employed for green function calculation noting that this model leads to less travel time residual times at distant stations and the most variance reduction of the real waveforms comparing to more local Hatzfeld model. To be added, inversion is performed in two steps. First seeking for the best position in a vertical grid with the epicenter relocated formerly starting at 1km depth with 1km vertical interval between each node for the main shock and 2km vertical interval for other inverted shocks (ending at 30 km). Secondly, seeking is continued over a horizontal grid at chosen depth in the previous step with 25 nodes that are posed differently for each event. All the stations waveforms are band-pass filtered across a retrieved frequency range separately for the sake of data quality and reaching more variance reduction.

<i>Depth(Km)</i>	<i>P-Velocity(Km/s)</i>	<i>V<sub>p</sub> / V<sub>s</sub>, 1.77</i>
0	5.38	
7	5.95	
12	6.15	
20	6.42	
47	8.06	
<i>IRSC</i>		
<i>Depth(Km)</i>	<i>P-Velocity(Km/s)</i>	<i>V<sub>p</sub> / V<sub>s</sub>, 1.77</i>
0	4.66	
11	5.84	
19	6.13	
46	8.1	
<i>Hatzfeld</i>		
<i>Depth(Km)</i>	<i>P-Velocity(Km/s)</i>	<i>V<sub>p</sub> / V<sub>s</sub>, 1.73</i>
0	5.38	
6	5.95	
14	6.15	
18	6.42	
46	8.05	
80	8.1	
<i>INSN</i>		

**Table 3.1.** Comparison of IRSC, Hatzfelds velocity models with the one used in IIEES results.

### 3.2.2. Seismic source inversion results for chosen events

In this section, all the results gathered for point-source inversion of the main shock is presented. Error estimation and investigating the stability of the results are performed in addition to rupture geometry. Finally, all the results with their error estimation are presented for 10 chosen events to reach a viewpoint on the rupture process over the region of impact. Main shock of the seismic sequence is relocated at 51.55 East Longitude , 28.46 North Latitude occurring at 11:52:48 UTC in the border of Khaki anticline close to Shonbeh city, based on the results of Nonlinear method. Considering the moment magnitude of the shock (6.4 Mw), it is reasonable to have some complexity in the rupture process, so that existing a sub-event and incompatible point source assumption with the real nature of the rupture process.

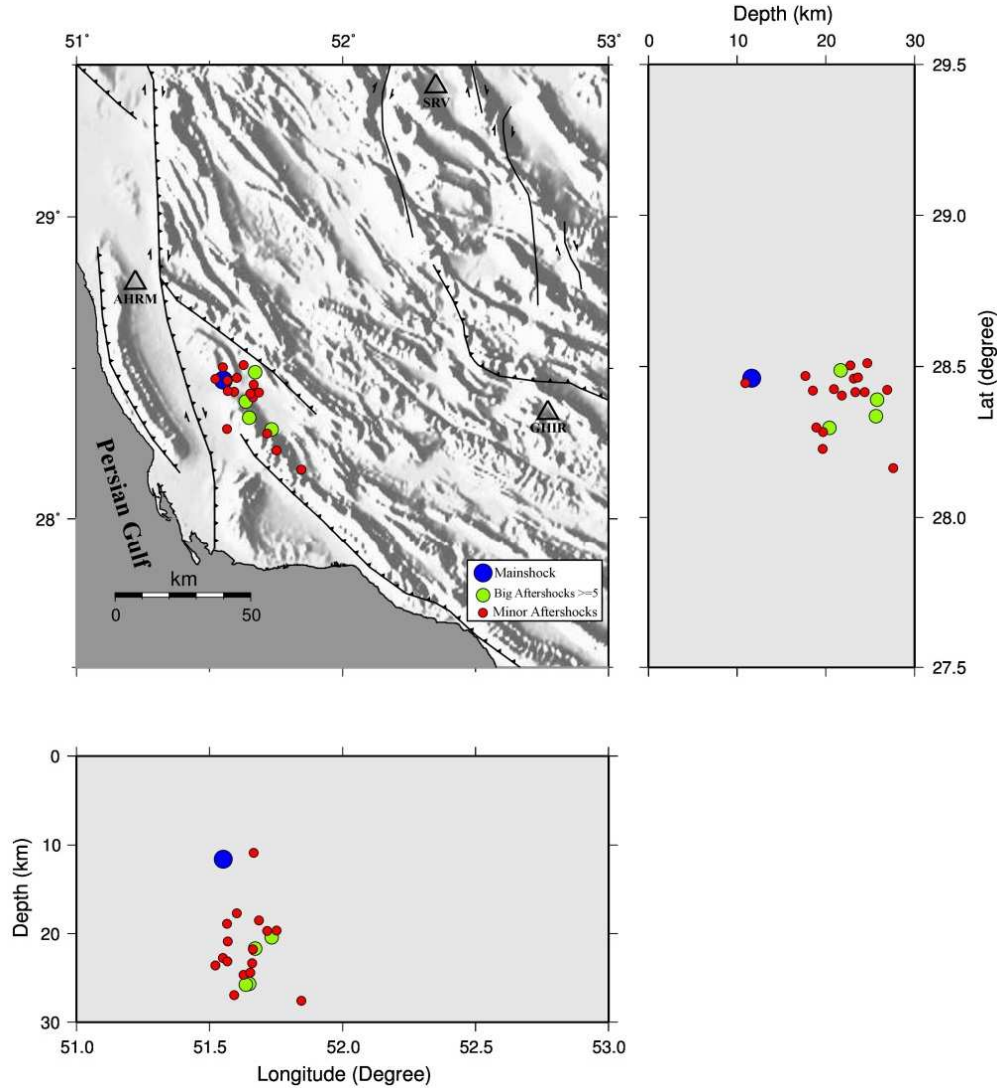


**Figure 3.2.1.** Chosen events for the point-source inversion with  $M_w \geq 4.5$ .

First seismic source geometry inversion is performed assuming a single event for the shock, then this assumption would be investigated carefully for reaching more certainty of the results and following analysis. Considering different quality of recorded data and existing noise for each station, chosen stations are shown in figure 3.2.2.

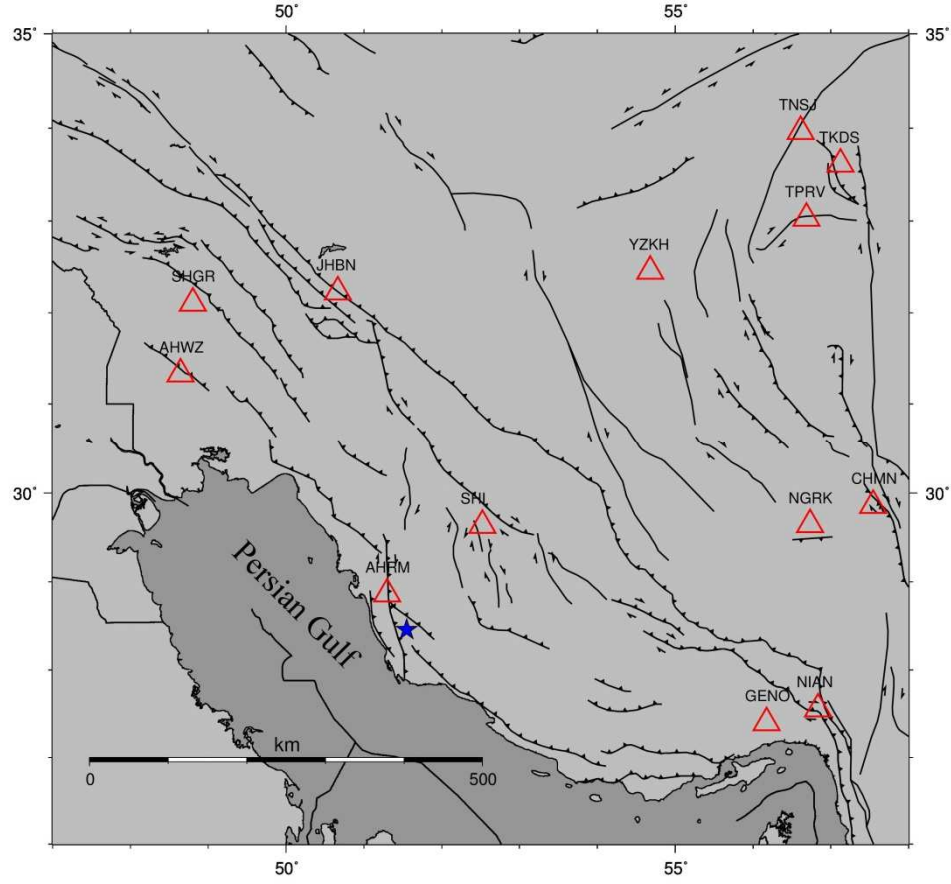


**Figure 3.2.2.** All the stations used for main shock forward waveform modeling.

Comparing calculated green functions with recorded data processed and band pass filtered within various frequency ranges, appropriate frequency ranges for each station to be utilized in inversion task are retrieved. (Table 3.2)

Station ID	Down Freq. (Hz)	Up Freq. (HZ)
AHRM	0.02	0.06
SHI	0.02	0.07
AHWZ	0.03	0.07
JHBN	0.03	0.07
GENO	0.02	0.05
SHGR	0.03	0.05
NGRK	0.03	0.04
NIAN	0.03	0.06
YZKH	0.02	0.05
CHMN	0.02	0.04
TPRV	0.02	0.05
TNSJ	0.03	0.06
TKDS	0.02	0.05

**Table 3.2.** Frequency range suitable for each station considering the result of waveform band-pass filtering.

To start up inversion, one vertical grid at the relocated epicenter with 15 nodes spread in 1km depth interval starting at 5km and ending in 19km is established. Afterwards, choosing the best depth, a horizontal grid of 25 nodes with 2km distance between each node is examined.

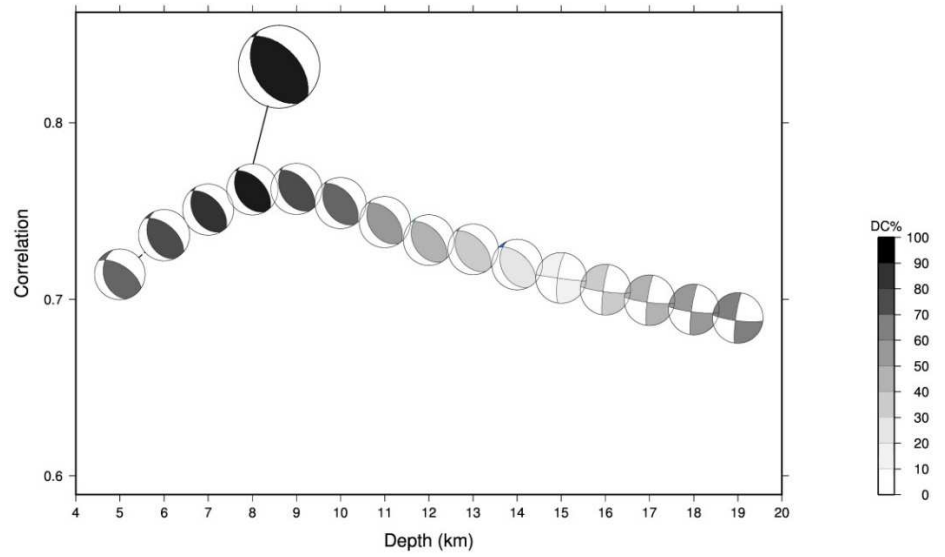


**Figure 3.2.3.** Inversion result of the main shock focal mechanism onto the vertical profile.

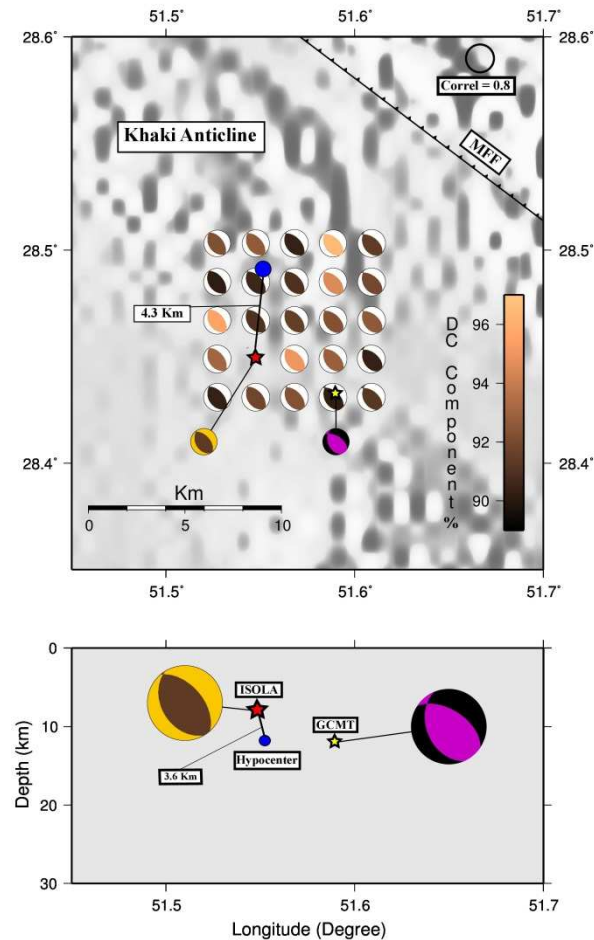


**Figure 3.2.4.** Inversion result for the main shock focal mechanism onto the horizontal grid placed at 8km depth. Focal spheres are colored based on DC value and their size suggests the correlation between observed and modeled waveforms. GCMT results are also depicted for comparison.

Regarding figure 3.2.4, horizontal distance between inverted centroid and the relocated epicenter is 4.3 km. To be added, inverted source geometry presents a reverse slip vector with a minor strike-slip component. Furthermore, inverted depth of centroid is 8 km that presents the initiation of the sequence at the lower-most part of the sedimentary cover. Considering the horizontal position of centroid comparing to the relocated hypocenter, spreading of the sequence to the southeast can be viewed explicitly in accordance with former relocation and GCMT results.

	Time (GMT)	Lat (°)	Long (°)	Depth (Km)	Varred %	DC %	M <sub>w</sub>	Max <sub>eig</sub> / Min <sub>eig</sub>	Str1 (°)	Dip1 (°)	Rake1 (°)	Str2 (°)	Dip2 (°)	Rake2 (°)	Centroid Time (Sec)
ISOLA	20130409/11 52 52.61	28.449	51.547	8	70	91.4	6.4	7.479	149	38	98	318	52	83	4.53
GCMT	20130409/11 58 54.5	28.27	51.62	12	-	100	6.3	4.317	157	41	117	303	54	69	4.6

**Table 3.3.** Final point-source inversion results in comparison with GCMT result.

### 3.2.2.1 Sub-event inspection

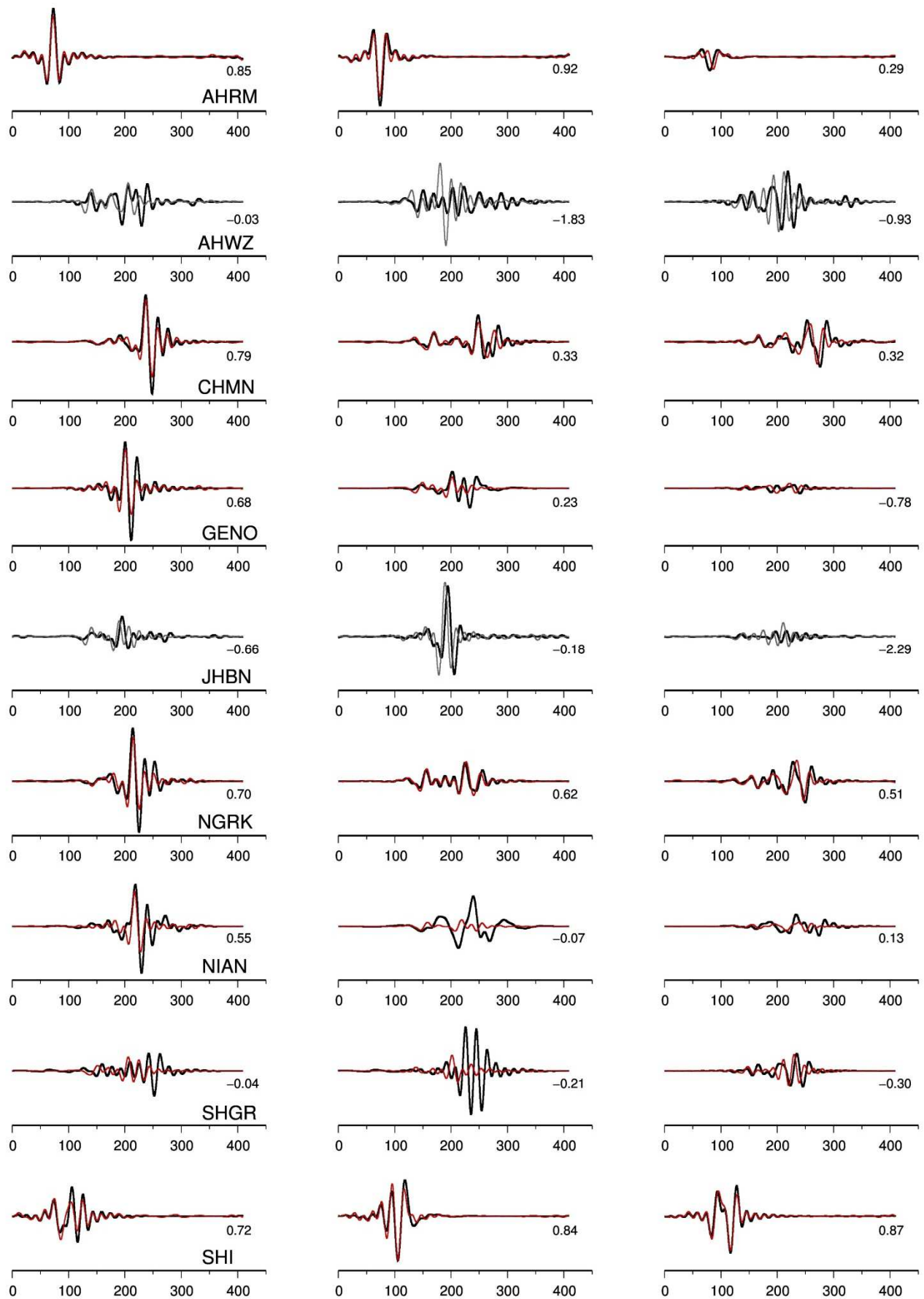
Being aware of the causative fault geometry, we intend to investigate any possible complexity through the rupture process. So that an oblique fault plane grid with 151° strike and 36° dip including 25 nodes that are spaced 0.5 km in dip direction and 2 km in the strike direction is established. This grid can somehow simulate the true fault plane. The origin node of the grid is to be centroid retrieved before, and is placed onto the 1<sup>st</sup> node (dip direction) and 2<sup>nd</sup> node (strike direction). Through this grid, all the nodes would be inverted for the possible sub-event for the main shock.

In table 3.4, inversion task is performed in three steps over possible causative fault plane. First, table 3.4 (a), inversion is executed assuming single event and deviated moment tensor that leads to an acceptable variance reduction and considerable double couple component and seismic moment magnitude. Regarding these three factors, any possible sub-event can be inspected carefully.

Secondly, table 3.4 (b), one possible sub-event is assumed through the inversion. Nevertheless variance reduction alters scarcely, and inverted slip vector is not compatible with the main event (normal component comparing to the reverse slip of the main event). In consequence, the assumption of having 2<sup>nd</sup> sub-event for the shock is rejected. Also this inspection is performed for 2 sub-event possibility (table 3.4 (c)), that again is declined for the same reasons mentioned. After this examination, we intend to investigate the stability and uncertainty of the solution assuming single event main shock.

### 3.2.2.2 Stability and uncertainty of reached modeling

Considering different quality of recorded data and disparity existing between the one dimensional velocity model and the true complex velocity structure (so that consequent green functions with the least uncertainty), seismic source inversion can be highly affected by removing one or more stations data from the inversion process. Specifically, when the stations are situated over seismotectonically different areas, so that different velocity layers, removing one station data with the most disparity of the velocity structure



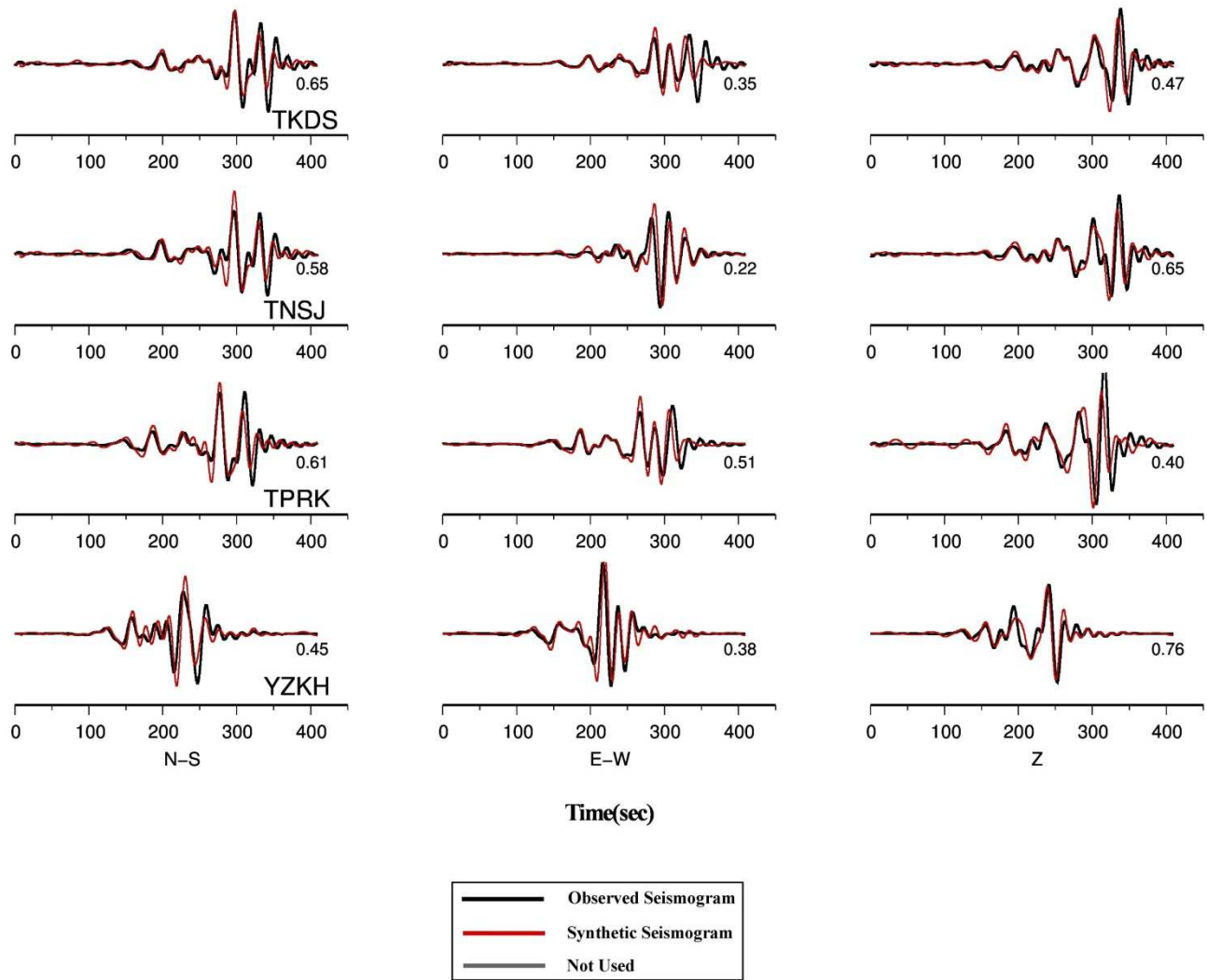


**Figure 3.2.5.** Observed and modeled waveforms taken out the main shock point-source inversion.

comparing to one used in the inversion can certainly affect results. Presently we intend to remove each station data, one by one, and investigate the consequent results for more examination of quality of the seismic source modeling. It is respected to reach the most affected results while removing the stations with both the most and least correlations, for the use of L2 norm in the correlation calculation. Results are shown as histograms in figure 3.2.7.

	Varred %	DC %	Centroid Depth (Km)	M <sub>o</sub> (Nm)	M <sub>w</sub>	Max <sub>eig</sub> / Min <sub>eig</sub>	Str (°)	Dip (°)	Rake (°)	Centroid Time (Sec)
Single Event	73	90.8	8.6	4.57E+18	6.4	11.63	149	37	99	7.5

(a)

	Varred %	DC %	Centroid Depth (Km)	M <sub>o</sub> (Nm)	M <sub>w</sub>	Max <sub>eig</sub> / Min <sub>eig</sub>	Str (°)	Dip (°)	Rake (°)	Centroid Time (Sec)
Subevent 1	72	77.3	8.4	4.09E+18	6.3	11.26	152	36	105	7.8
Subevent 2	74	75.8	8.9	6.73E+17	5.8	12.51	149	67	-91	12.85

(b)

	Varred %	DC %	Centroid Depth (Km)	M <sub>o</sub> (Nm)	M <sub>w</sub>	Max <sub>eig</sub> / Min <sub>eig</sub>	Str (°)	Dip (°)	Rake (°)	Centroid Time (Sec)
Subevent 1	69	75.3	8.00	3.97E+18	6.3	6.84	149	36	100	8.1
Subevent 2	71	80	8.9	7E+17	5.8	6.84	148	38	-84	17.65
Subevent 3	72	74.7	8.6	4.81E+17	5.7	6.75	152	40	-78	7.8

(c)

**Table 3.4.** Inversion result of the main shock assuming One, two and three sub-events considering an oblique grid with strike and dip similar to the probable causative fault. Results suggest the main shock to feature single event.

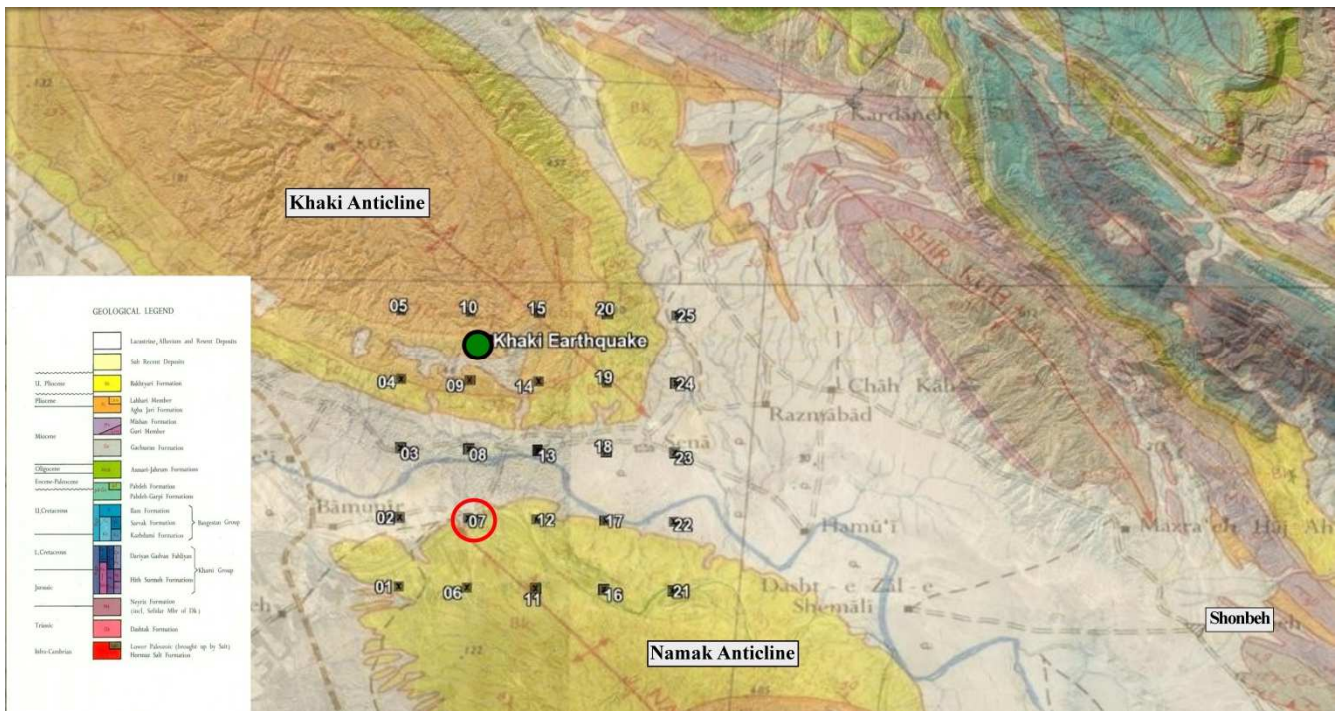


**Figure 3.2.6.** Geometrical distribution of the horizontal grid considered for main shock point-source inversion on the geological map of region. As seen in the figure, rupture is distributed toward southeast.

Regarding figure 3.2.7 (e), slip vector certainly shows a reverse motion, as all the inverted slip vectors for two possible fault planes present such this motion. In figure 3.2.7 (f), suspected some complexity of the rupture process is noticeable regarding little DC components retrieved in the inversion for each step.

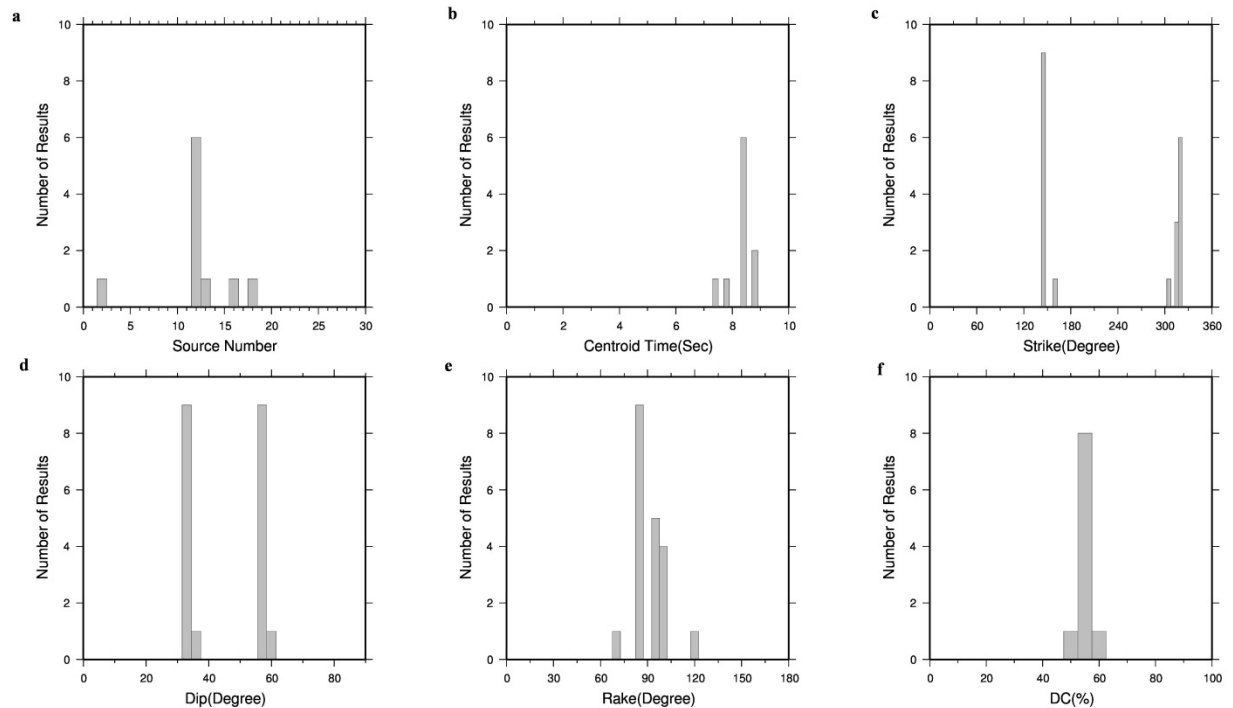


**Figure 3.2.7.** Results of the stability test for final inversion result. One station is removed for each step.

Nevertheless more inspections show very little difference in the value of variance reduction and correlation for the results with much more DC component. Also removing AHRM station, one with the most correlation with the calculated waveforms, lowers DC component considerably, resulting of low DC being nonsense.

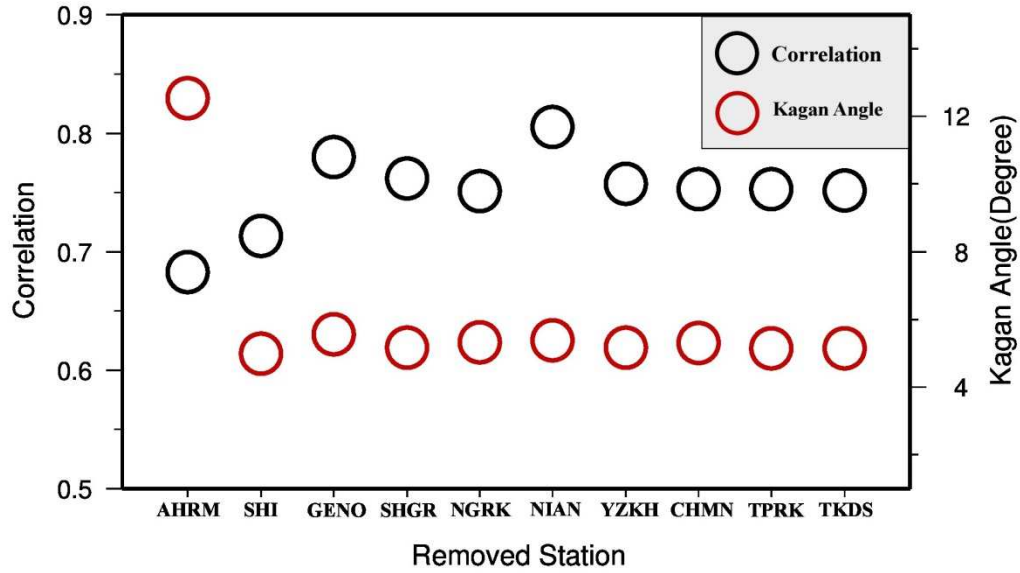


**Figure 3.2.8.** Distribution of all correlation values for each step with the relevant Kagan angle.

Regarding figure 3.2.8, fluctuation of the correlation between observed and calculated waveforms is not considerable except for two stations AHRM and SHI. As the substantial impact of these two stations onto the final variance reduction, removing each one from inversion process can highly affect the results. As mentioned before, the function to calculate variance reduction is L2-norm, meaning that removing the stations data with the little correlation can lead to considerable increase of final variance reduction, as seen for the stations NIAN, SHGR and GENO.

Moreover little Kagan angle [12] changes can be viewed in figure 3.2.8, so that little changes of the inverted source parameters and consequent stable optimum solution. Nevertheless removing AHRM data leads to  $12^\circ$  Kagan angle. This again presents the substantial impact of removal of a station with the most effect on the final variance reduction and the resulted source parameters. Considering much correlation between calculated and observed waveforms for this station, its removal certainly leads to the considerable change in the inverted source parameters to reach a suitable variance reduction. In figure 3.2.9, all the inverted source parameters are shown onto the focal sphere regarding each station removal.

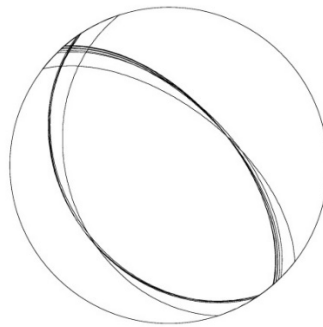


**Figure 3.2.9.** Point-source solution on the focal sphere for each step of stations removal.

### 3.2.2.3 Error estimation of the source parameters without waveform inversion

In this section, we attempt to determine stability of the resulted source parameters employing Zahradnik and Custodio method [12], that is to reach the estimation without any further inversion of the models in vicinity of the results. This method seems rapid and efficient for inspection of too much models in vicinity of the optimum results. First, a threshold value for variance reduction must be set. Afterwards, all the double-couple moment tensors (zero determinant and trace) are retrieved as resulting variance reduction in the range of threshold value and optimum value. To acquire better grasp of the distribution of these moment tensors over the model space, converting to geometrical source parameters is executed.

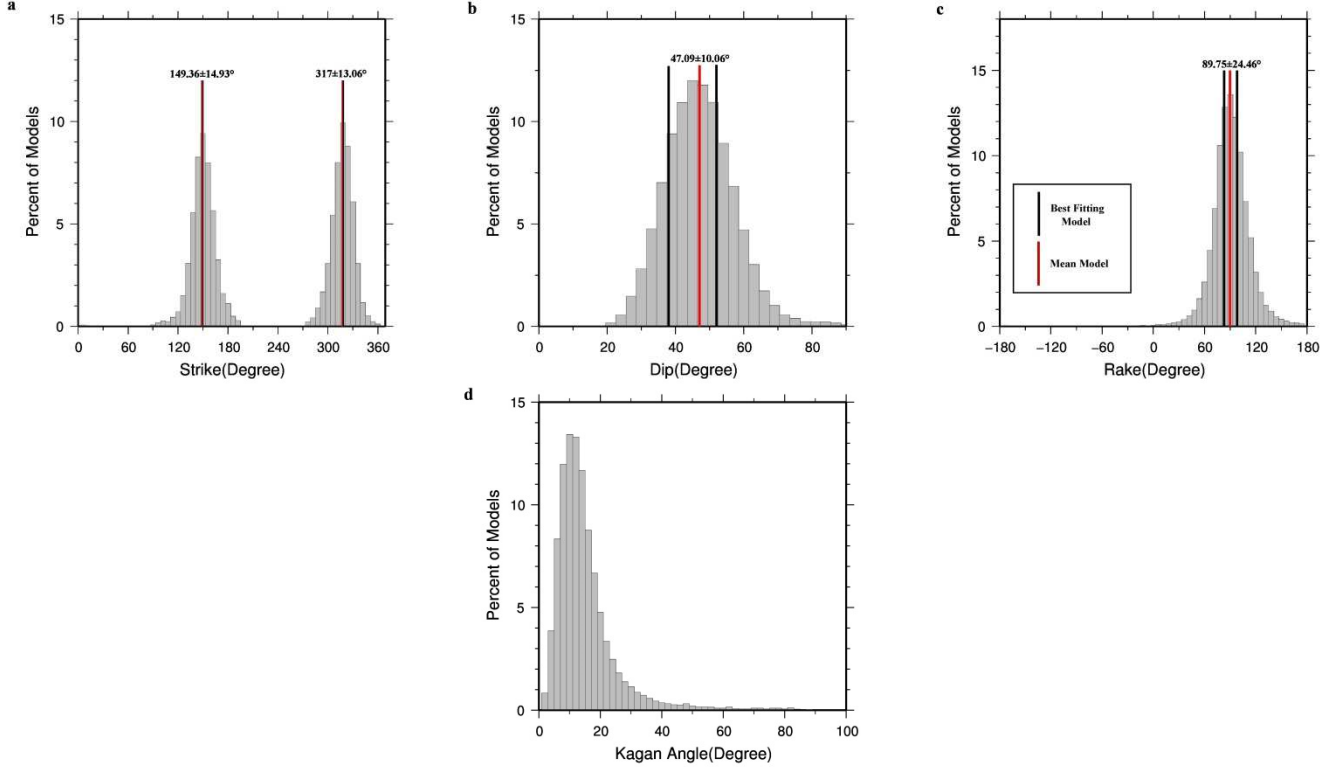


**Figure 3.2.10.** Histogram of the models parameter in vicinity of the optimum solution. 10 percent difference of correlation is considered to specify the sampled models. Also Kagan angle histogram of the picked models is shown (d).

C is set as 2 (relation (113) in ref [12]), resulting real data error threshold value of variance reduction is acquired by setting  $\Delta\chi^2 = 1$  (relation 15). Afterwards, all the DC models over the retrieved variance reduction interval are resulted and converted to the pertinent geometrical source parameters. All the resulted models are shown on a focal sphere and are depicted as histograms as following. As an interesting mark, less scattering of the models in vicinity of optimum model is respected, then larger value of variance reduction interval, in the case of stable inverted optimum model. As seen in figure 3.2.10 (a-d), distribution of the source parameters relevant to the models in vicinity of the optimum models presents a Gaussian behavior that suggests using standard deviation to estimate error of the resulted models. For dip and slip vector, one pick can be distinguished as two fault plane solutions are close. In result, mean value gets spaced from the optimum models of two fault planes. Furthermore, mean value of Kagan angle also is calculated as 14 degrees. It is important to note that distribution of the models around the optimum one is acquired by use of 10 percent of variance reduction interval comparing to the best solution.

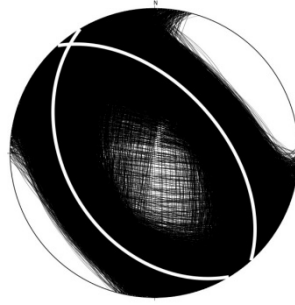


**Figure 3.2.11.** Focal mechanisms of all 69712 DC models in vicinity of the optimum model.

The number of inspected models and standard deviation of each source parameter and Kagan angle are shown in the table 3.5.

Str1 Str1_mean Str1_std	Str2 Str2_mean Str2_std	Dip1 Dip_mean Dip_std	Dip2 Dip_mean Dip_std	Rake1 Rake1_mean Rake1_std	Rake2 Rake2_mean Rake2_std	Kagan_mean(°)	Number_models	Data Variance	Varred_interval (%)	C
149 149.36 14.93	318 317 13.06	38 47.09 10.06	52 47.09 10.06	98 89.75 24.46	83 89.75 24.46	14.68	69712	2.295E-9	10	2

**Table 3.5.** Average focal parameters and relevant standard deviation are shown for all the models in vicinity of the optimum solution.

Using the approach mentioned above, theoretical error estimation of other 10 aftershocks are retrieved and consequently their inverted solutions are selected, as shown in table 3.6.

### 3.3. Seismotectonic model of the region

Having the point source inversion results of 21 events with  $M_w \geq 4.5$ , we intend to reach a unified model describing the rupture process injected by this seismic sequence. Considering the dominant effect of error estimation of inverted depth for the events, centroid depths of the events are selected for the final conclusion, instead of relocation results. Also for some elemental events such as Qeshm earthquake (2005,  $M_w$  5.8), Fin earthquake (2006,  $M_w$  5.7) and Bam earthquake (2003,  $M_w$  6.6) a distinctive difference between relocated and centroid depth is clearly seen, so that our approach seems to be reasonable.

Considering a cross section with 60 degree azimuth (perpendicular to the probable causative fault), centroid depth and epicenter of 11 events with variance reduction greater than 55 percent is shown (Figure 3.3.1). Looking at the figure, all the events are colored based upon their initiation time from the main shock, consequently the migration of rupture from northwest to the southeast of the fault plane can be distinguished. Also examining the model of displacement data recorded by satellite (INSAR) over two weeks after the initiation of the main shock, we expect to have bigger shocks in the southeastern part of the rupture plane. Noting the loss of sufficient seismic energy compatible with the recorded displacement over this part, aseismic activity can be modelled for the dominant displacement over the southeastern part of the fault plane. All the inverted centroids depict southward dip with depths included in the range of 8 – 12 km, suggesting 4 km width of epicentral region of the events. Also we propose a 40 km long region of impact for the sequence. The dominant rupture geometry is reverse with no explicit sign of the rupture over the ground. In result, this sequence features somehow the hidden shear sources. Based on the CMT solutions, depth range of the rupture is limited to 8-12 km suggesting that the dominant seismic energy is confined to the uppermost part of the bedrock and the lowermost part of the sedimentary layer. Also the sedimentary layer depth is proposed to be 12 km for this region [13]. Noting

the rupture depth, Hormoz salt unit can be responsible for the stoppage of the rupture distribution in depth. Finally considering the slip vector of the biggest aftershock and some other elemental aftershocks, a minor left-lateral strike slip component can be in addition considered as the rupture mechanism.

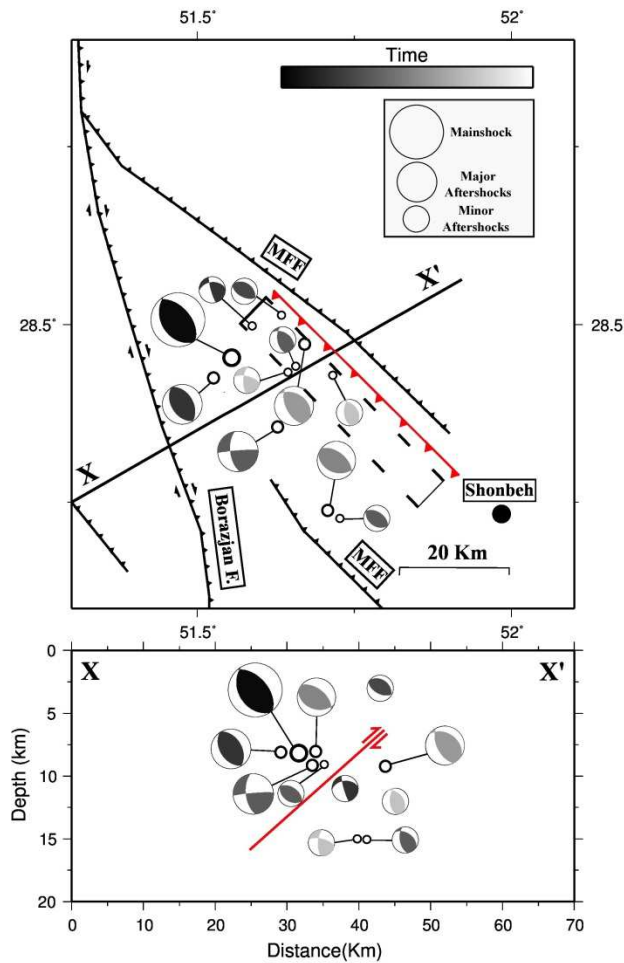


**Figure 3.3.1.** 11 focal mechanisms retrieved for the events with at least 55% correlation between observed and modeled waveforms. Focal spheres are colored base on the time of occurrence relative to the main shock. As it can be seen, reverse motion with minor left-lateral strike slip component is considered as the dominant slip vector injected into the region of impact with a southward dip for the principle fault plane. Rupture length is estimated 40 km with 4km width as the epicentral rupture region.

## 4 Acknowledgement

We took advantage of thoughtful suggestions along with fruitful discussions with Dr. Oveisi, as he is excessively familiar with the geology and seismotectonics of the region. After that, we are thankful for all the endeavors Dr. Gheytaichi devoted for the completion of this work.

Time (GMT)	Lat (°)	Long (°)	Depth (Km)	Varred %	DC %	M <sub>0</sub>	Centroid Time (Sec)	CN	Str1 Str1_mean Str1_std	Str2 Str2_mean Str2_std	Dip1 Dip1_mean Dip1_std	Dip2 Dip2_mean Dip2_std	Rake1 Rake1_mean Rake1_std	Rake2 Rake2_mean Rake2_std	Kagan_mean (°)	Number_models	Plane_1 Num_mod	Plane_2 Num_mod	Data Variance	Varred Interval	C	Chosen Plane	Focal Mechanism
20130409/11 52 52.61	28.449	51.547	8	70	91.4	6.4	7.55	7.479	149 149.36 14.93	318 317 13.06	38 47.09 10.06	52 47.09 10.06	98 89.75 24.46	83 89.75 24.46	14.68	69712	69984	69184	6.935E-5	10	2	1	
20130409/12 47 50.8	28.498	51.587	11	69	91.5	4.7	2.8	1.924	164 161.62 7.01	264 267.56 9.30	81 77.11 6.933	41 37.68 8.41	130 126.38 9.485	13 17.997 14.93	13.65	115884	101324	112152	3.539E-9	1.481	2	1	
20130409/13 30 45.25	28.555	51.564	13	54	81.8	4.3	0.78	4.9	273 273.25 8.57	168 167.04 7.23	47 47.139 9.68	74 73.55 7.89	21 22.32 12.48	135 134.45 10.32	14.09	107276	107258	103286	1.825E-10	0.21	2	2	
20130409/14 44 56.58	28.474	51.598	13	54	74.9	4.4	2.28	4.33	174 175.32 9.84	305 306.26 10.5	59 59.65 6.67	42 43.00 7.31	120 120.83 9.59	49 49.53 11.44	12.98	108044	54020	54016	5.356E-10	0.22	2	1	
20130409/16 32 34.58	28.513	51.635	3	64	72.8	4.5	0.68	8.72	307 312.17 15.7	117 120.51 15.98	35 41.45 10.05	54 54.45 10.25	97 100.39 23.80	84 83.13 22.44	20.12	21718	20324	20952	1.578E-9	0.12	2	2	
20130409/20 54 19.9	28.434	51.67	15	53	71.6	4.6	1.2	3.53	161 161.97 9.23	324 324.34 10.36	51 52.75 4.07	39 39.35 4.38	100 100.91 8.07	76 75.86 9.33	10.15	118308	118246	115100	9.013E-10	0.59	2	1	
20130410/01 58 28.4	28.24	51.635	9	64	72.5	5.4	0.84	1.925	173 172.473 5.79	265 272.37 6.12	60 58.17 9.10	86 75.91 8.10	175 162.67 10.62	29 33.66 10.00	14.3	143656	116302	115820	3.77E-7	0.64	2	1	
20130410/07 10 41.87	28.228	51.727	9	56	50.1	5.0	2.07	1.745	125 115.55 15.46	304 316.00 11.58	40 36.23 4.99	49 57.74 6.40	91 72.77 18.45	88 101.70 12.56	13.57	140628	139260	140488	2.21E-8	3.42	2	1	
20130410/08 00 3.1	28.442	51.653	19	62	70.3	5.2	2.50	2.017	170 176.43 7.84	303 297.42 8.24	56 59.98 7.22	44 49.13 7.65	121 130.13 9.08	51 42.29 9.89	12.28	113744	113742	113744	5.737E-8	5.38	2	1	
20130410/19 22 54.26	28.227	51.785	9	51	97.9	4.4	0.96	2.56	311 311.21 9.64	101 100.52 12.77	57 59.60 5.81	35 35.90 5.34	106 107.32 10.14	65 63.92 15.25	11.91	155404	155284	154492	2.562E-10	3.11	2	2	

**Table 3.6.** Theoretical error estimation is depicted for the focal mechanism of 10 events with the optimum final solution for each one. In this table, we try to choose the principle plane of incidence based on the result of theoretical error estimation of point-source solution of the events.

## 5 References

- [1] Berberian M., 1995. Master "blind" thrust faults hidden under the Zagros folds: active basement tectonics and surface morphotectonics, *Tectonophysics*, 193-224, **241**.
- [2] Ambraseys, N., and Melville C. P., 1982. A History of Persian Earthquakes. Cambridge University Press, **219**.
- [3] Lomax A.J. Virieux P., Berge C., 2000. Probabilistic earthquake location in 3D and layered models: Introduction of a Metropolis-Gibbs method and comparison with linear locations, in *Advances in Seismic Event Location* Thurber, C.H., and N. Rabinowitz (eds.), Kluwer, Amsterdam, 101-134.
- [4] Hatzfeld D., Tatar M., Priestley K., Ghafory-Ashtiany M., 2003. Seismological constraints on the crustal structure beneath the Zagros Mountain belt (Iran): *G. J. Int.* **155**, 403–410.
- [5] Shomali Z. H., Keshvari F., Hassanzadeh J. and Mirzaei N., 2011. Lithospheric structure beneath the Zagros collision zone resolved by non-linear teleseismic tomography. *Geophysical Journal International*, **187**(1), 394-406.
- [6] Tatar M., Hatzfeld D. and Ghafory-Ashtiany M., 2004. Tectonics of the Central Zagros 997(Iran) deduced from microearthquake seismicity, *GJI*, **156**, 255–266.
- [7] Nissen E., Tatar M., Jackson J. A. and Allen M. B., 2011. New views on earthquake faulting in the Zagros fold-and-thrust belt of Iran, *GJI*, **186**, 928–944.
- [8] Yamini-Fard F., Hatzfeld D., Tatar M., Mokhtari M., 2006. Microearthquake Seismicity at the intersection between the Kazerun fault and the Main Recent Fault (Zagros, Iran). *Geophysical Journal International*, **166**, No. 1, 186-189.
- [9] Zahradnik J., Serpetsidaki A., Sokos E. and Tselentis G. A., 2005. Iterative Deconvolution of Regional Waveforms and a Double-Event Interpretation of the 2003 Lefkada Earthquake, Greece. *B. Seismol. Soc. Am* 159-172, **95**.
- [10] Zahradnik J., Gallovic F., Sokos E., Serpetsidaki A. and Tselentis A., 2008. Quick fault-plane identification by a geometrical method: Application to the Mw 6.2 Leonidio earthquake, 6 January 2008, Greece. *Seismological Research Letters*, **79**(5), 653-662.
- [11] Bouchon M., 1981. A simple method to calculate Green's functions for elastic layered media, *B. Seismol. Soc. Am*, 959-971, **71**.
- [12] Zahradník J. and Custódio S., 2012. Moment tensor resolvability: Application to southwest Iberia. *Bulletin of the Seismological Society of America*, **102**(3), 1235-1254.
- [13] Oveisi B., Lavé J., Van Der Beek P., Carcaillet J., Benedetti L. and Aubourg C., 2009. Thick-and thin-skinned deformation rates in the central Zagros simple folded zone (Iran) indicated by displacement of geomorphic surfaces. *Geophysical Journal International*, **176**(2), 627-654.